White Rose Research Online

eprints@whiterose.ac.uk
https://eprints.whiterose.ac.uk
Universities of Leeds, Sheffield and York

Deposited via The University of Sheffield.

White Rose Research Online URL for this paper:
https://eprints.whiterose.ac.uk/id/eprint/193868/

Version: Accepted Version

Article:
Hussain, G., Ahmed, I., Rehman, A.U. et al. (2022) Study of the role of dysprosium substitution in tuning structural, optical, electrical, dielectric, ferroelectric, and magnetic properties of bismuth ferrite multiferroic. Journal of Alloys and Compounds, 919. 165743. ISSN: 0925-8388

https://doi.org/10.1016/j.jallcom.2022.165743

Article available under the terms of the CC-BY-NC-ND licence (https://creativecommons.org/licenses/by-nc-nd/4.0/).

Reuse
This article is distributed under the terms of the Creative Commons Attribution-NonCommercial-NoDerivs (CC BY-NC-ND) licence. This licence only allows you to download this work and share it with others as long as you credit the authors, but you can't change the article in any way or use it commercially. More information and the full terms of the licence here: https://creativecommons.org/licenses/

Takedown
If you consider content in White Rose Research Online to be in breach of UK law, please notify us by emailing eprints@whiterose.ac.uk including the URL of the record and the reason for the withdrawal request.

UNIVERSITY OF LEEDS
University of Sheffield
UNIVERSITY of York

Study of the role of dysprosium substitution in tuning structural, optical, electrical, dielectric, ferroelectric, and magnetic properties of bismuth ferrite multiferroic

Gulzar Hussain[1], Ishfaq Ahmed[1], Atta Ur Rehman[2], Muhammad Umair Subhani[1], Nicola Morley[3], Maria Akhtar[2], Muhammad Imran Arshad[2], and Hafeez Anwar[1]*.

[1]Department of Physics, University of Agriculture, Faisalabad, 38040, Pakistan.
[2]Department of Physics, Government college university, Faisalabad, 3800, Pakistan.
[3]Department of Materials Science and Engineering, The University of Sheffield, S1 3JD, UK
*Corresponding author's E-mail: hafeez.anwar@gmail.com

Abstract

Magnetoelectric multiferroics, which combine ferroelectric and magnetic characteristics, have potential use in a variety of electronic devices. In this work, Dy^{3+} substituted bismuth ferrites with the chemical formula $Bi_{1-x}Dy_xFeO_3$ (x = 0.0, 0.15, 0.30, 0.45, and 0.60) were synthesized using the sol-gel auto combustion process. The effect of Dysprosium substitution in $BiFeO_3$ (BFO), on its structural, surface morphology, optical, electrical, dielectric, ferroelectric, and magnetic properties were studied. The rhombohedral perovskite structure of the space group (*R3c*) was confirmed *via* X-ray diffraction (XRD) analysis. Moreover, the crystallite size had a maximum value of 59.57 nm for x = 0.30. XRD and FTIR confirmed the substitution of Dy^{3+} into BFO ferrite. Further, the structural change and absorption bands confirmed the substitution of Dy^{3+} ions into the lattice. For x = 0.30, the energy bandgap of 2.81 eV was found. The resistivity and activation energy were minimum and drift mobility was maximum at x = 0.30 as compared to Dy^{3+} doped BFO samples. At low frequency, the dielectric loss was reduced, while at high frequency, the dielectric loss increased with increasing frequency. The saturated polarization (P_S), electric polarization (E_C), and remnant polarization (P_r) have values of 6.95 μC/cm^2, 3.49 μC/cm^2, and 1.53 kV/cm for x = 0.30, respectively. The maximum saturation magnetization and microwave frequencies were 10.89 emu/g and 2.41 GHz, respectively at Dy^{3+} concentration x = 0.30. These materials are suitable for electronic and microwave devices.

Keywords: rhombohedral; dysprosium; absorption bands; polarization; magnetization.

1 Introduction

Materials having multifunctional characteristics have recently caught the interest of a large community of scientists due to their potential use in different fields of physics and technology. Multiferroic materials have two or more ferroic characteristics, such as Ferro-/ferri-/antiferromagnetism, Ferro-elasticity, and ferroelectricity. Some of them have the additional characteristic of being able to adjust their magnetization in an electric field, as well as modify their electrical properties in the existence of an applied magnetic field. This is known as the magnetoelectric (ME) effect [1]. Because of their multifunctional uses in sensors [2], spintronic devices [3], non-volatile memory applications [4], and energy harvesting applications [5], these materials have obtained huge attention. Bismuth ferrite is G-type ferrite and belongs to the *R3c* space group with a distorted ABO_3 type crystal structure [6, 7]. Even though it has interesting properties, its practical use is limited due to the formation of secondary phases during its synthesis. These phases cause unfavorable properties, such as high current leakage, structural distortion, low tangent loss, and weak magneto-electric interaction. As a result, the structural, dielectric, electrical, ferroelectric, and magnetic characteristics of the $BiFeO_3$ (BFO) material are affected [8, 9]. Several techniques are employed to synthesize magnetic materials including the sol-gel route [10], the coprecipitation method [11-14], the citrate precursor method [15, 16], the hydrothermal process [17], the solid-state reaction technique [18], the liquid-phase sintering [19], etc. The citrate precursor technique is known to be the ideal procedure for preparing BFO due to its time savings, limited computation temperature, and ease to control stoichiometry [20]. Basiri *et al*., [21] prepared La substituted bismuth ferrite ($Bi_{1-x}La_xFeO_3$) at (x = 0.0, 0.10, 0.15 and 0.20) *via* sol-gel technique. The structural studies demonstrated that La-doping enhances asymmetry while decreasing the second phase. The spin cycloid distortion enhances the magnetic characteristics of the La^{3+}, according to the magnetic measurements. Sati *et al*., [22] found with increasing the Eu^{3+} content, the optical band-gap decreases from 2.25 to 2.16 eV, plus there was an increase in the frequency-independent area of dielectric constant and Dielectric loss, such that the dielectric properties improved. Mishra *et al*., [23] used a metal ion ligand complex-based precursor-solution vaporization technique to fabricate Y^{3+} substituted $BiFeO_3$ (BFO) nanocrystalline samples. In Y^{3+} substituted BFO, the loss tangent was reduced, and the magnetic parameters were improved by increasing the Y^{3+} concentration. At room temperature (RT), a switching behavior in the field dependence of magnetization was seen in all the samples, and this

behavior was found to improve with increasing Y^{3+} content. Dhir *et al*., [24] prepared $Bi_{1-x}Dy_xFeO_3$ (x = 0.0, 0.10) *via* the sol-gel technique, and reported the peaks shift with the substitution of Dy^{3+} ions. The synthesized nanoparticles confirmed the ferromagnetic behavior. The magnetization saturation was 2.56 emu/g for x = 0.10. Arora *et al*., [25] reported Dy^{3+} substituted bismuth ferrites (BFO) nanoparticles by using the sol-gel auto combustion method. In all the samples, the dielectric analysis revealed two important dimensions of interaction around the Neel temperature. With rising Dy^{3+} concentration, the conductivity of the samples decreased suggesting suppression of oxygen vacancies. Sati *et al*., [26] reported the effect of Dy^{3+} substitution on optoelectronic and magnetic properties of $BiFeO_3$. The distortion in rhombohedral FeO_6 octahedra is characterized by a decrease in lattice parameters and unit cell volume up to x = 0.12, with no evidence of phase transition. The weak ferromagnetic hysteresis loops and maximum remnant magnetization (Mr) was 0.2103 emu/g for x = 0.12.

In present work, we have prepared Dy^{3+} substituted $BiFeO_3$ by auto combustion method with concentration (x = 0.00, 0.15, 0.30, 0.45 and 0.60). After that, the impact of Dy^{3+} substitution on structural, optical, electrical, dielectric, ferroelectric, and magnetic characteristics are studied. Dy^{3+} was selected because of its stability and tendency for ferromagnetic interaction. Furthermore, it is anticipated that substituting Dy^{3+} at the B-site would result in improved structural, optical, electrical, dielectric, ferroelectric, and magnetic properties. The prepared samples are characterized using XRD, SEM, EDX, FTIR, UV-vis spectroscopy, electrical, dielectric, ferroelectric, and magnetic measurements respectively.

2. Experimental work

High purity chemicals such as Bismuth Nitrate [Bi $(NO_3)_3.5H_2O$], Ferric Nitrate [Fe $(NO_3)_2.9H_2O$], Dysprosium Nitrate [Dy $(NO_3)_3$. xH_2O], Citric acid ($C_6H_8O_7$), Nitric acid (HNO_3), and Ammonia solution were used. Distilled water was used as a solvent. All the chemicals were weighed precisely inappropriate stoichiometric amounts and were dispersed in a 0.5 M solution of distilled water. Dilute (HNO_3) was added dropwise until a clear solution was achieved. The citric acid concerning metal nitrate (1:1) used for fuel agents was mixed into the solution. The prepared solution was heated on a hot plate at 318 K. Ammonia solution was used to maintain pH at 7. After this, the temperature was increased from 383 K until the sample was converted into a gel and then the temperature increased up to 573 K. Continuous heating produced a viscous dry gel, which was further burned to produce ash. The gel ash was ground in

a mortar pestle and then sintered at 873 K for 3 hours. The synthesis procedure is shown in Fig. 1.

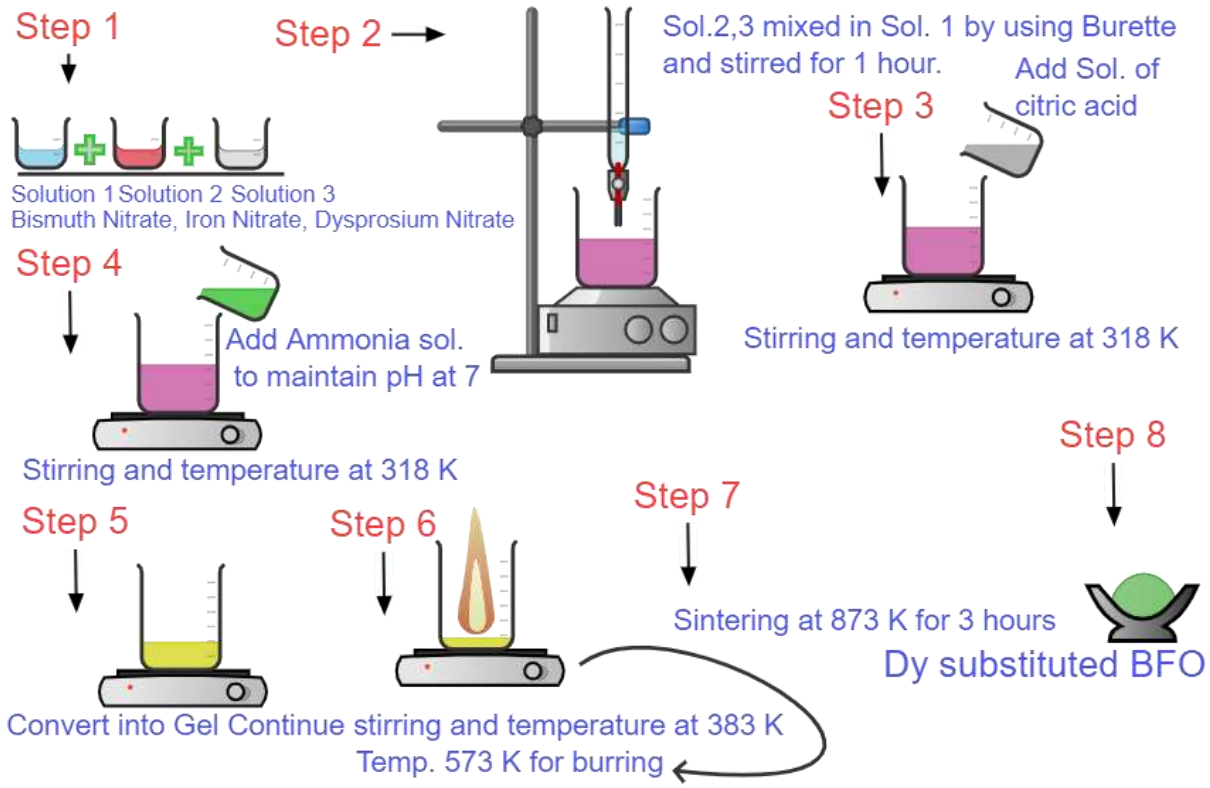

Fig. 1 Sol-gel auto combustion synthesis procedure of Dy^{3+} substituted Bismuth ferrites

3. Characterizations

The structural characteristics of Dy^{3+} substituted BFO samples were studied using X-Ray Diffraction (XRD) utilizing Cu Kα (λ = 1.5418 Å) with a scanning angle range of $20° \leq 2\theta \leq 80°$ and a scanning rate of 2°/min. The morphology of the prepared materials was studied with a scanning electron microscope (SEM) JEOL-JSM 5910 and the EDX spectrometer was used for elemental analysis. The absorption bands were characterized using a Perkin Elmer FTIR spectrometer. At RT, a UV-visible spectrometer PG (Model T-80) was used for optical measurements in the wavelength (λ) range of 200 – 800 nm. The DC electrical resistivity was determined through the I–V measurement Technique (Keithley Model 2400) in the temperature range of 313 K – 773 K. The dielectric measurements were taken using the IM3536 series LCR Meter at RT Magnetic properties were measured using a vibrating sample magnetometer (VSM) with a field applied of ±6000 Oe (Model VSM-175).

4. Results and discussions

4.1 Structural analysis of Dy^{3+} substituted BFO ferrites

Fig. 2 (a) shows the XRD patterns of Dy^{3+} substituted BFO ferrites and confirmed the rhombohedral perovskite structure with space group (*R3c*). The peaks of BFO ferrite are labeled with miller indices (012), (104), (110), (202), (024), (116), (214), (300) and well-suited with JCPDS card no. 01-086-1518. Besides the formation of rhombohedral structures, a few secondary phases were also formed. The peaks labeled with (310) and (141) belong to $Bi_2Fe_4O_9$ having space group (*Pbam*) (JCPDS card no. 01-072-1832). Further, with the substitution of Dy^{3+} ion in the rhombohedral matrix, the $DyFeO_3$ peaks were observed and indexed with the planes (101) and (111) corresponding to the JCPDS card no. 01-089-6645. For Dy^{3+} concentration x = 0.15 to x = 0.60, the peak Dy_2O_3 correspond to the plane (222) and well-matched with JCPDS card no. 00-043-1006. The peak represented by the symbol (&) is for the $Bi_{25}FeO_4$ phase [27] and the peak labeled with the symbol (♦) corresponds to Bi_2O_3. It was noted that when Dy^{3+} ions were added to the $BiFeO_3$ matrix, the intensity of the impurity peaks decreased and that the peaks (104) and (110) were displaced to a lower angle, as seen in Fig.2 (b). This might be attributed to the replacement of Dy^{3+} ions in the BFO lattice, which prevents the formation of impurity phases, which resulted in phase transitions from the rhombohedral to the orthorhombic structure. This distortion has also been detected in other rare-earth-substituted $BiFeO_3$ (BFO) [28-30]. As a result of the difference in ionic radii of Dy^{3+} (0.92 Å) and Bi^{3+} (0.117 Å). For Dy^{3+} doping x = 0.15 in BFO ferrite Cyriac *et al.*, [31] observed two phases including $BiFeO_3$ and $Bi_2Fe_4O_9$ phases, while for Dy^{3+} doping they observed the $BiFeO_3$ phase along with Dy_2O_3 and $DyFeO_3$ phases. Fig. 3 (a) showed the ball-and-stick unit cell structure and Fig. 3 (b) revealed the polyhedral unit cell structure of as-prepared $BiFeO_3$ ferrite. Similarly, Fig. 4 (a) showed the ball-and-stick unit cell structure, and Fig. 4 (b) revealed the polyhedral unit cell structure of as-prepared $Bi_{0.85}Dy_{0.15}FeO_3$ ferrite. The interplanar spacing (d) was determined using relation (1) [32, 33];

$$d = \frac{n\lambda}{2sin\theta} \qquad (1)$$

where n = 1 for first-order diffraction. The calculated values are given in Table 1. The average crystallite size (D) was calculated by using Scherer's method given in equation (2) [33];

$$D = \frac{k\lambda}{\beta cos\theta} \qquad (2)$$

Where k = 0.94 (crystalline shape factor), λ = 0.015418 nm (the wavelength of X-ray), and β represent the full width at half maximum respectively while θ is the angle of diversion [27]. The crystallite size (D) has a minimum value of 28.80 nm for x = 0.0 and maximum value of 59.57 for x= 0.30 (Table 1). The following relation was used to calculate lattice constants (a and c);

$$\frac{1}{d^2} = \frac{4}{3}\left[\frac{h^2+hk+k^2}{a^2}\right] + \frac{l^2}{c^2} \qquad (3)$$

where h, k, l represents Miller indices [25]. The unit cell volume (V) of bismuth ferrites having hexagonal structure i.e., $a = b \neq c$ and $\alpha = \beta = 90^{o}$ and $\gamma = 120^{o}$ were calculated and are given in Table 1. In this study, the lattice constant (a) and (c) are also given in Table 1. The variation in the lattice parameters may be due to the substitution of Dy^{3+} (0.92 Å) ions along with Bi^{3+} (0.117 Å) ions.

Table 1 Lattice parameters of the as-prepared samples

Dy^{3+} Concentration (x)	**0.00**	**0.15**	**0.30**	**0.45**	**0.60**
Interplanar Spacing d_{hkl} (Å)	2.3292	2.2930	2.2923	2.3785	2.2433
Crystallite size D (nm)	28.80	57.86	59.57	54.97	48.89
Lattice constant a (Å)	5.5900	5.6091	5.6195	5.6128	5.6089
Lattice constant c (Å)	13.8823	13.8453	13.8749	13.8830	13.8394
Unit cell volume V ($Å^3$)	375.68	377.08	379.43	378.75	376.78
Nelson-Riley Function F (θ)	1.1878	1.3894	1.3890	1.4194	1.3180
X-ray density d_X (g/cm^3)	8.2963	8.2529	8.1897	8.1921	8.2227
Bulk density d_B (g/cm^3)	0.8323	0.8295	0.8219	0.8222	0.8251
Porosity percentage ($P\%$)	89.97	89.96	89.96	89.97	89.98
Specific surface area S (m^2/g)	25.11	12.56	12.31	13.32	14.92
Packing factor (p)	12.37	25.23	25.98	23.11	21.79
Strain (ε)	0.1843	0.1909	0.1903	0.1767	0.1987
Dislocation density $\delta \times 10^{-4}$ (nm^{-2})	2.1	2.9870	2.8180	3.3093	4.1836

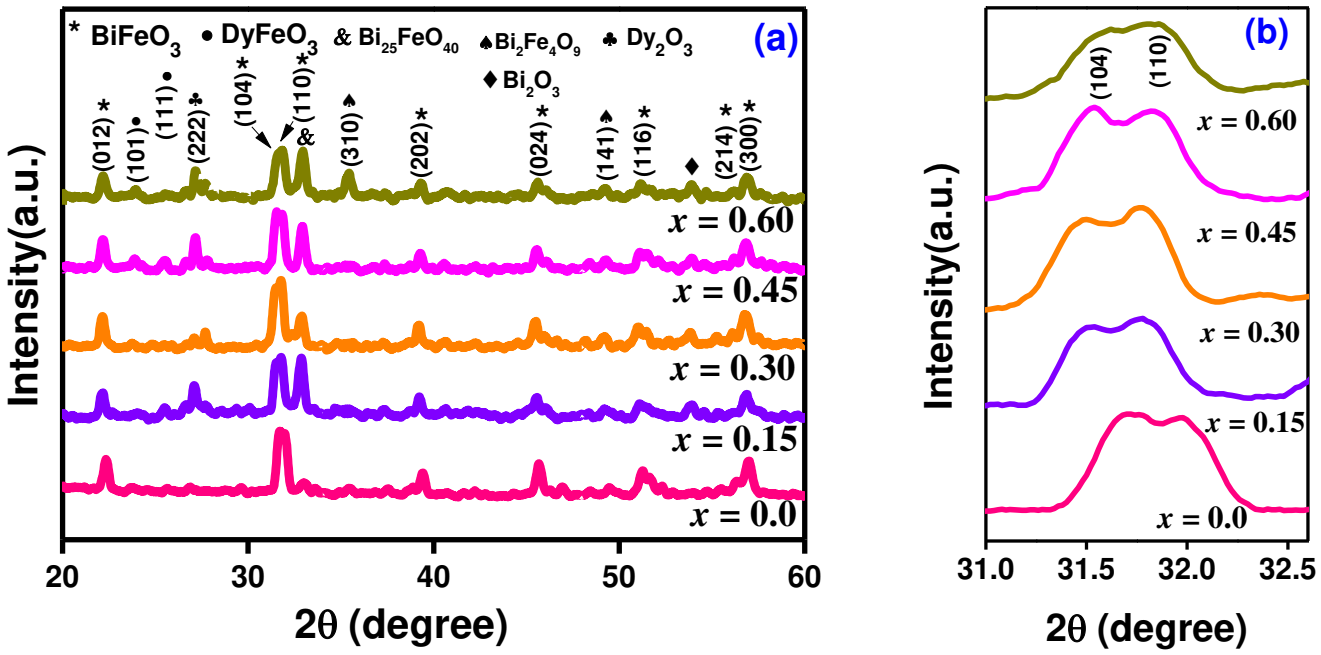

Fig. 2 (a) XRD patterns of as-prepared samples and **(b)** enlarged view of the plane (104) and (110) for all the samples

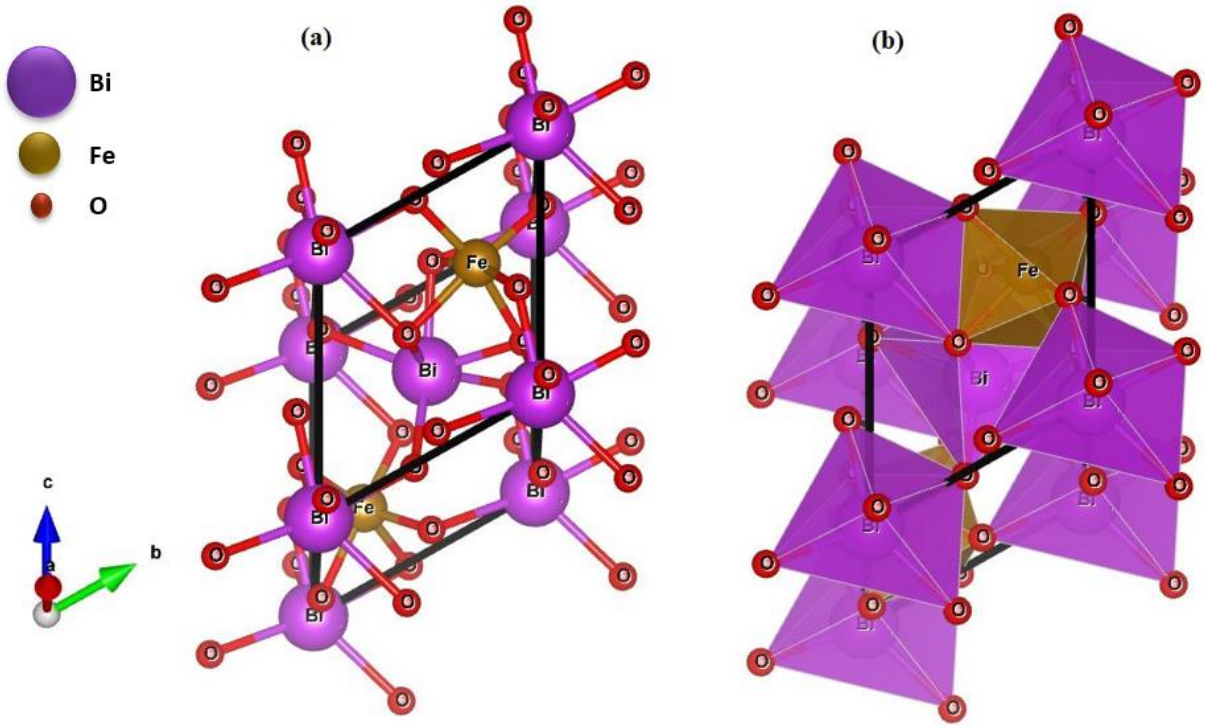

Fig. 3 (a) Ball-and-stick unit cell structure **(b)** Polyhedral unit cell structure of as-prepared *BiFeO*$_3$ ferrite

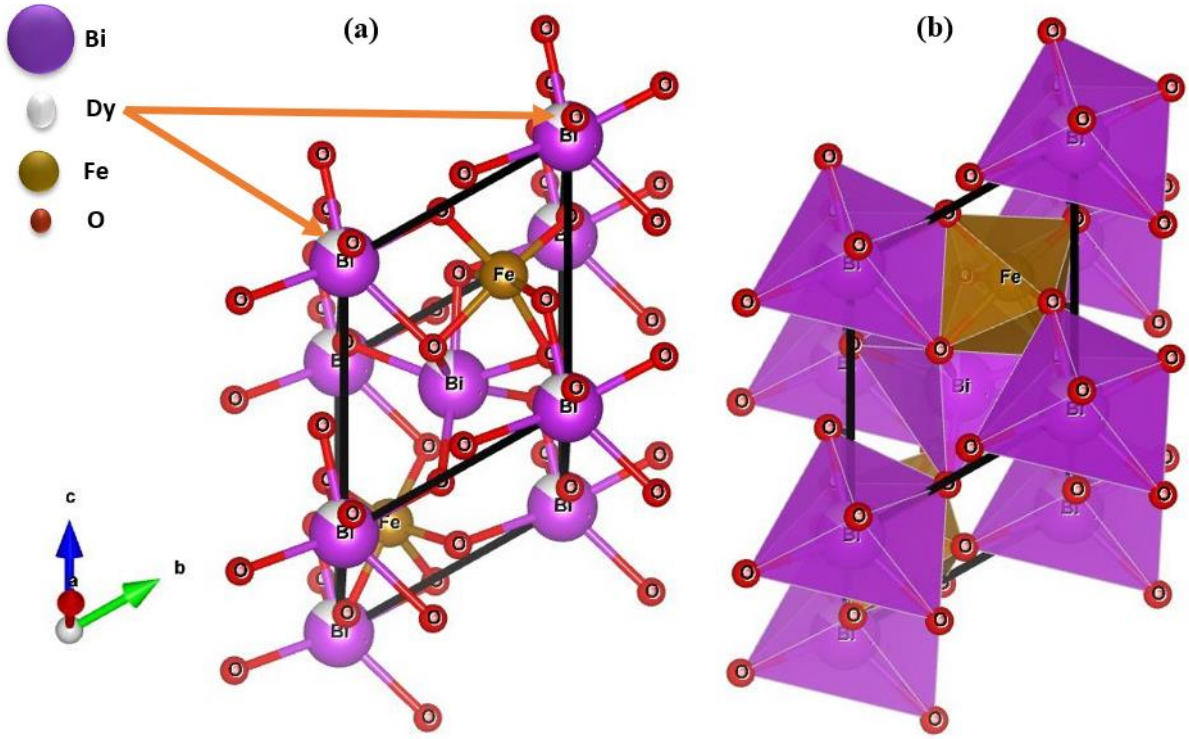

Fig. 4 (a) Ball-and-stick unit cell structure **(b)** Polyhedral unit cell structure of as-prepared $Bi_{0.85}Dy_{0.15}FeO_3$ ferrite

Moreover, equation (4) was used to find out Nelson-Riley function $F(\theta)$ [33];

$$F(\theta) = \frac{1}{2}\left[\frac{cos^2\theta}{sin\theta} + \frac{cos^2\theta}{\theta}\right] \quad (4)$$

The values of $F(\theta)$ were given in Table 1. The $F(\theta)$ decreased from 1.1878 to 1.3890 for $x = 0.0$ to $x = 0.30$ and has a maximum value of 1.4194 for $x = 0.45$. The lattice constants increase then decrease slightly with Dy^{3+} replacement because Dysprosium penetrates the $BiFeO_3$ lattice. In other words, the increase and decrease in the value of the lattice parameters are attributed to the addition of smaller sized Dy^{3+} (0.92 Å) as compared to Bi^{3+} (0.117 Å). However, the variation in the lattice parameters is also due to the various impurity phases that are always formed during synthesis, together with $BiFeO_3$ as the main phase due to the kinetics of formation [34]. The X-ray density (d_X) and bulk density (d_B) were determined using relations (5) and (6) [35, 36], respectively.

$$d_X = \frac{6M}{N_A \times V} \quad (5)$$

$$d_B = \frac{Mass}{Volume} = \frac{M}{\pi r^2 \times h} \quad (6)$$

where N_A = 6.022 × 10^{23}, *M, h,* and *r* represent the molecular weight of the composition, thickness, and radius of the pellet. The porosity percentage (*P*%) was calculated using relation (7) [35];

$$P\% = \left[1 - \frac{d_B}{d_X}\right] \times 100 \qquad (7)$$

The estimated values of "d_X", "d_B" and "*P*%" are given in Table 1. It was observed from Table 1 that the "d_X" is larger compared to "d_B". This difference in density is caused by some inevitable pores to be produced during the sample synthesis and sintering process. The rise in density has been discovered to be dependent on the atomic weight of the ingredients. Because Bi^{3+} has a higher atomic weight (208.9 amu) than Dy^{3+}, its bulk density rises (162.5 amu) [28]. The relationships (8-11) were used to calculate the specific surface area (*S*), packing factor (*p*), strain (ε), and dislocation density (δ) [35], respectively.

$$S = \frac{6000}{d_X \times D} \qquad (8) \qquad P = \frac{D}{d} \qquad (9)$$

$$\varepsilon = \frac{1}{d^2} \qquad (10) \qquad \delta = \frac{1}{D^2} \qquad (11)$$

The maximum surface area was found to be 25.11 m^2/g for x = 0.0 and minimum value of 12.31 m^2/g for x = 0.30 (Table 1). Moreover, the packing factor has a minimum value of 12.37 for x = 0.0 and maximum value was 25.98 for x = 0.30. The minimum strain was found to be 0.1767 for x = 0.45. The dislocation density depends on the average crystallite size as shown in relation (11) therefore, dislocation density has maximum values for Dy^{3+} concentration x = 0.0.

4.2 Morphological and compositional analysis

Fig. 5(a-c) shows micrographs of the as-prepared samples for x = 0.0, 0.3 and 0.6. It is observed that the pure and Dy^{3+} substituted BFO samples show an irregular shape, agglomeration, and non-uniform surface. With the replacement of Dy^{3+}, the aggregation was increased in the as-prepared samples. It may be due to the suppression of oxygen vacancies as a consequence of Dy^{3+} addition [37].

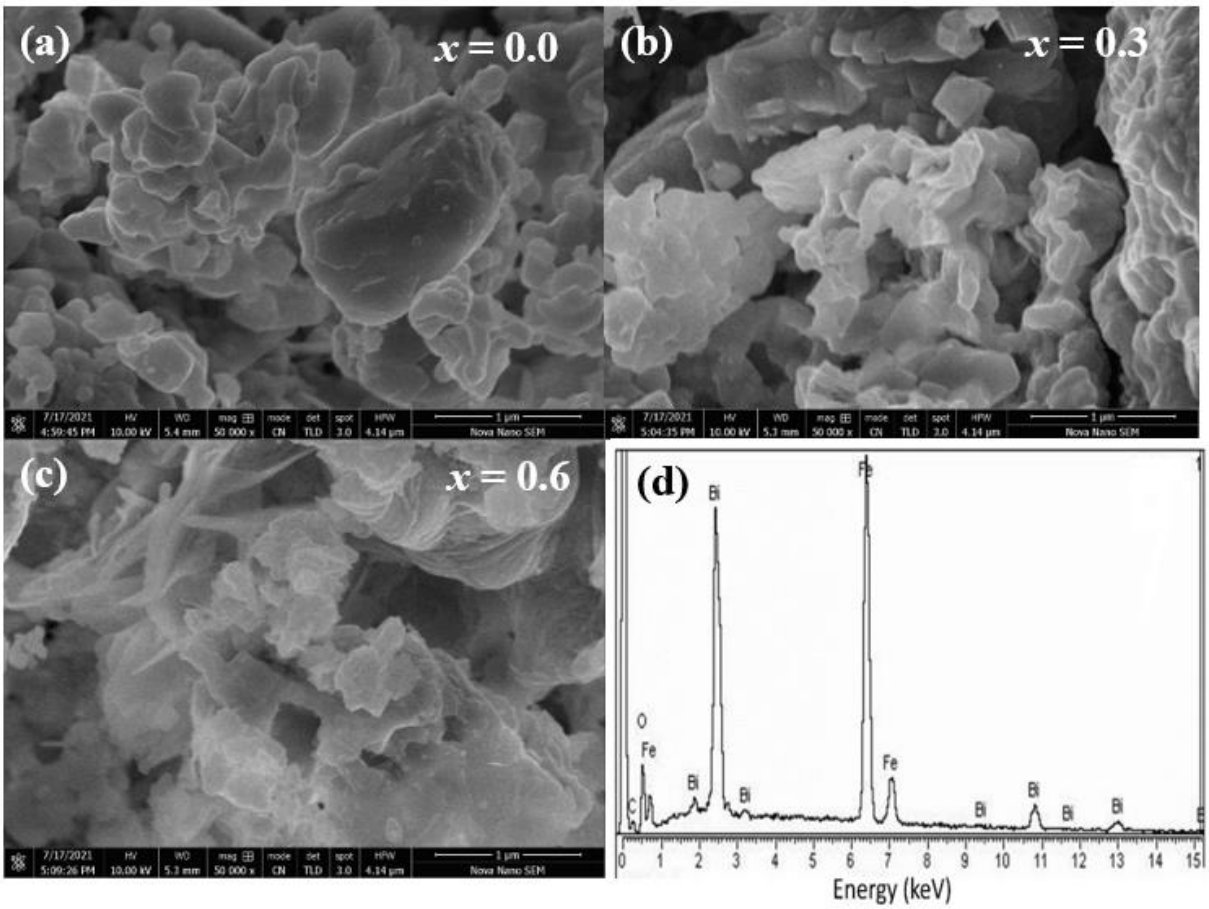

Fig. 5(a) SEM micrographs for samples x = 0.0 **(b)** SEM micrographs for samples x = 0.30 **(c)** SEM micrographs for samples x = 0.60 **(d)** EDX spectrum for sample x = 0.30

Fig. 5 (d) depicts the energy dispersive X-ray (EDX) spectrum of $Bi_{1-x}Dy_xFeO_3$. This analysis confirms the purity and existence of the constituent's parts, such as bismuth, iron, and oxygen, as well as their atomic ratios. Dysprosium peaks are not shown because our substitution concentration is very small.

4.3 Absorption band analysis of Dy^{3+} substituted $BiFeO_3$ ferrites

The FTIR spectra of the Dy^{3+} substituted $BiFeO_3$ powders x = 0.0, 0.30 and 0.60 are shown in Fig.6. The absorption peaks at 527 cm^{-1}, 533 cm^{-1} and 523 cm^{-1} for x = 0.00, x = 0.30 and x = 0.60. In perovskite materials, octahedral FeO_6 groups are connected with Fe–O stretching and bending vibrations [38]. The metal-oxygen band was characterized by another band that emerged around 821 cm^{-1}, 816 cm^{-1} and 812 cm^{-1} for (x = 0.0, 0.30 and 0.60), respectively. This confirmed the development of BFO highly crystalline phase *R3c* [39, 40].

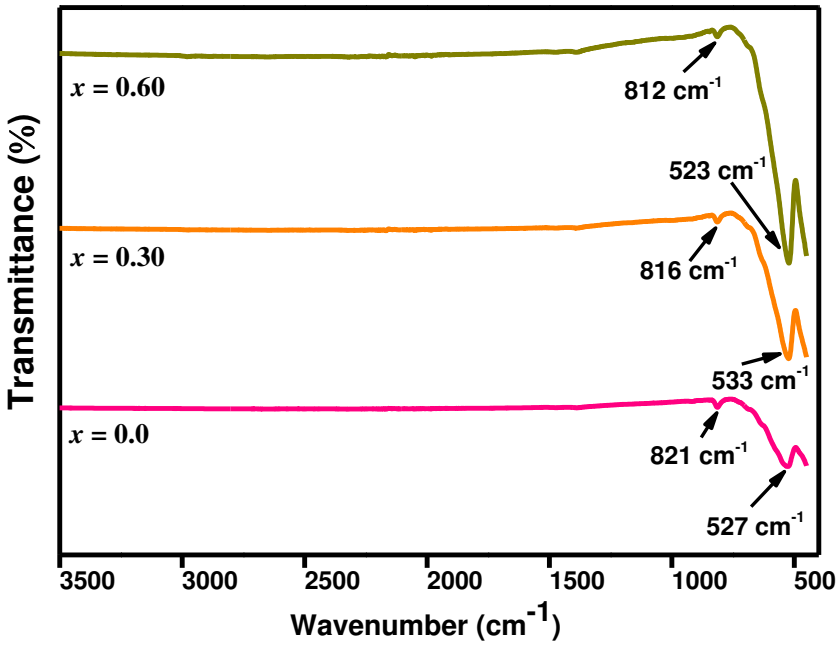

Fig. 6 Fourier transform infrared (FTIR) spectra of $Bi_{1-x}Dy_xFeO_3$ (x = 0.0, 0.30 and 0.60) for range 400 – 3500 cm^{-1}

4.4 Optical bandgap analysis of Dy^{3+} substituted $BiFeO_3$ ferrites

Fig. 7(a-c) shows the Tauc plots for the compositions x = 0.00, x = 0.30 and x = 0.60. The energy bandgap (E_g) is calculated using the relation [41];

$$\alpha h\nu = B(h\nu - Eg)^m \qquad (12)$$

where "$h\nu$" is photon energy and "B" is the transition probability dependence constant. In addition, "m" indicates the sort of transition. In the case of an indirect transition, m = 2, but in the case of a direct bandgap, m = 1/2. The energy bandgap (E_g) was decreased from 2.93 eV to 2.71 eV for the Dy^{3+} concentration x = 0.0, 0.3, and 0.60 (as seen in Fig. 7(a-c)). A similar decreasing trend of optical bandgap with the substitution of Dy^{3+} in BFO was reported by Sati *et al.*, [26]. Cyriac *et al.*, [31] reported 2.08 eV optical bandgap for Dy^{3+} doping x = 0.3 in BFO ferrite. The rearrangement of molecular orbitals and distortion caused in the FeO6 octahedra may be responsible for the decrease in bandgap [42].

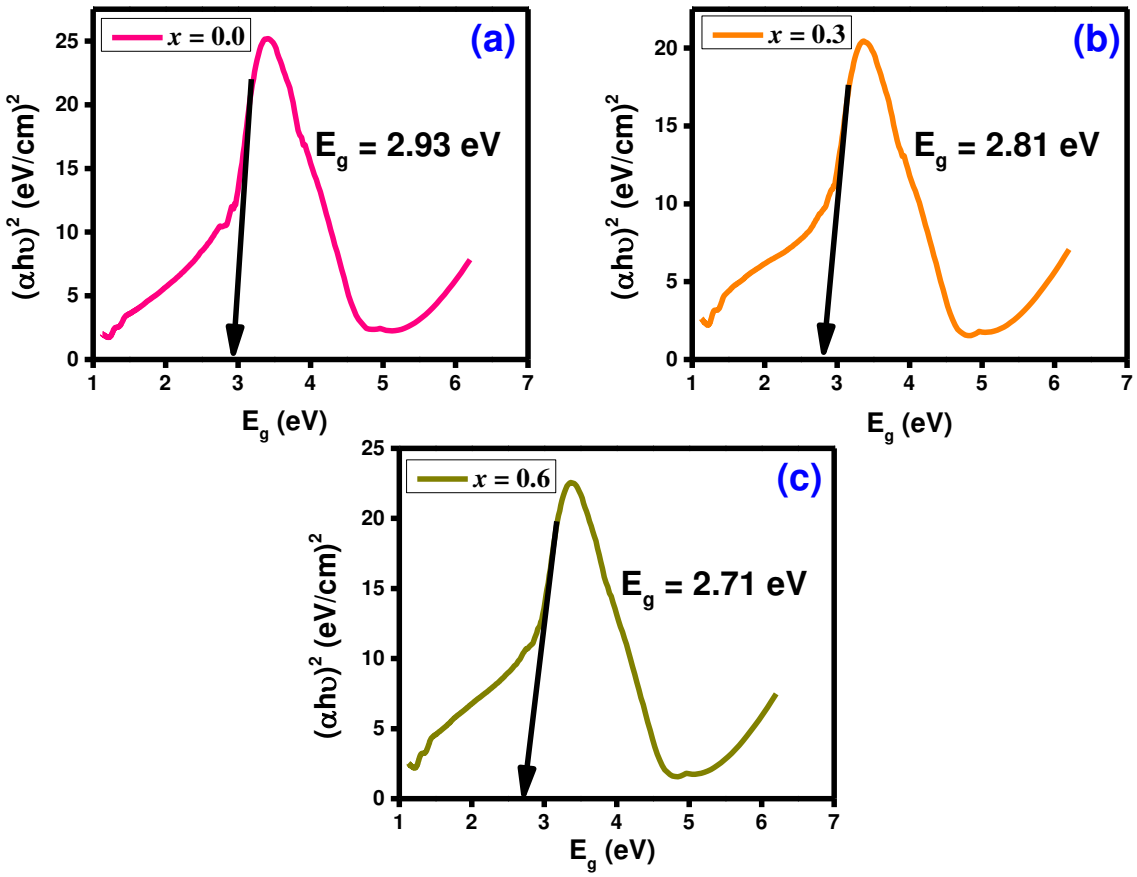

Fig 7 Tauc plots for the compositions x = 0.00, 0.30 and 0.60 of Dy^{3+} substituted BFO ferrites

4.5 Electrical properties of Dy^{3+} substituted $BiFeO_3$ ferrites

The Arrhenius plots (1000/T *versus* the log of resistivity) are displayed in Fig. 8. It is clear from Fig. 8 that each resistivity curve is divided into two regions. The Curie temperature is the temperature (T_C) at which the resistivity changes. Each plot in Fig. 8 is made up of two linear parts with distinct slopes and activation energies. This trend suggests that when the temperature rises, the sample's electrical conduction goes *via* two processes. The activation energies (Ea) of the produced samples were determined using the following formula [43];

$$E\text{a} = 2.303 \times k_B \times 10^3 \times \text{slope (eV)} \qquad (13)$$

where "k_B" Boltzmann constant (8.602× 10^{-5} eV/K). The activation energies at low temperature "E_{low}" and high temperature "E_{High}" were computed from the 1000/T *versus* the log of resistivity plots and their values are given in Table 2. For the same sample, "E_{Low}" is less than "E_{High}" (as seen in Table 2). The activation energy of the ionic conduction process caused by oxygen vacancies in perovskite-type ferroelectric oxides is low. In contrast, the energy band or hopping

mechanism of concentrated charge carriers is linked with large activation energy [44]. The drift mobility (μ_d) of the electrons can be determined using the following formula [35];

$$\mu_d = \frac{1}{\eta e \rho_{DC}} \quad (14)$$

where ρ_{DC} represents the DC electrical resistivity. "η" and "e" represents charge concentration and electric charge, respectively. The charge concentration is determined by applying the following formula [35];

$$n = \frac{N_A\, d_B\, P_{Fe}}{M} \quad (15)$$

where N_A, d_B, M, and P_{Fe} represent Avogadro's number, bulk density, molecular mass, and the Number of Fe atoms current in the composition. The maximum drift mobility was $1.947 \times 10^{-20} \pm 0.03$ cm^2/Vs for $x = 0.00$ and the minimum value of $0.150 \times 10^{-20} \pm 0.03$ cm^2/Vs was for $x = 0.15$ (as seen in Table 2 and Fig. 10). Fig. 9 depicted Dy^{3+} concentration *versus* the log of resistivity at different temperatures. It was observed from Fig. 10 and Table 2 that the maximum value of resistivity was $8.490 \times 10^8 \pm 0.03$ Ω cm for Dy^{3+} concentration $x = 0.15$ at 313 K. The maximum activation energy (Ea) for $x = 0.15$ was 0.1288 ± 0.03 eV, and the variation with Dy^{3+} concentration is shown in Fig. 10. The activation energy trend is similar trend with the DC resistivity trend.

Table 2 Electrical parameters of all the samples

x	$\rho_{DC} \times 10^8$ at 313 K ± 0.03 (Ω cm)	$\mu_d \times 10^{-20}$ ± 0.03 (cm^2/Vs)	T_C (K)	Activation Energy (eV) ± 0.03		
				E_{low}	E_{high}	$E_a = E_{high} - E_{low}$
0.00	0.667	1.947	342	0.0118	0.0491	0.0373
0.15	8.490	0.150	351	0.0024	0.1313	0.1288
0.30	0.775	1.621	342	0.0023	0.0105	0.0081
0.45	1.383	0.888	358	0.0024	0.0133	0.0108
0.60	1.675	0.713	373	0.0023	0.0159	0.0135

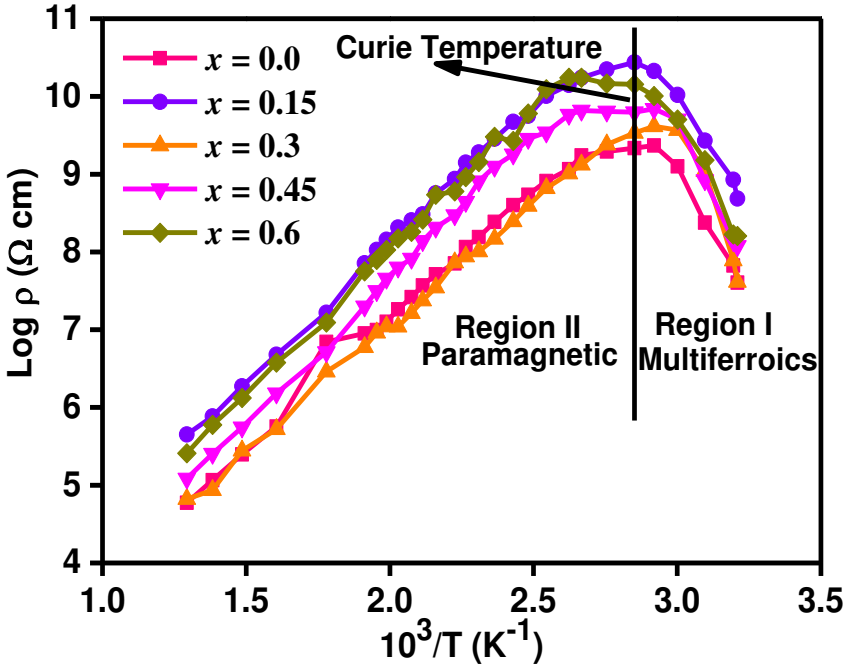

Fig. 8. Plots of 1000/*T versus* the log of resistivity for all the samples

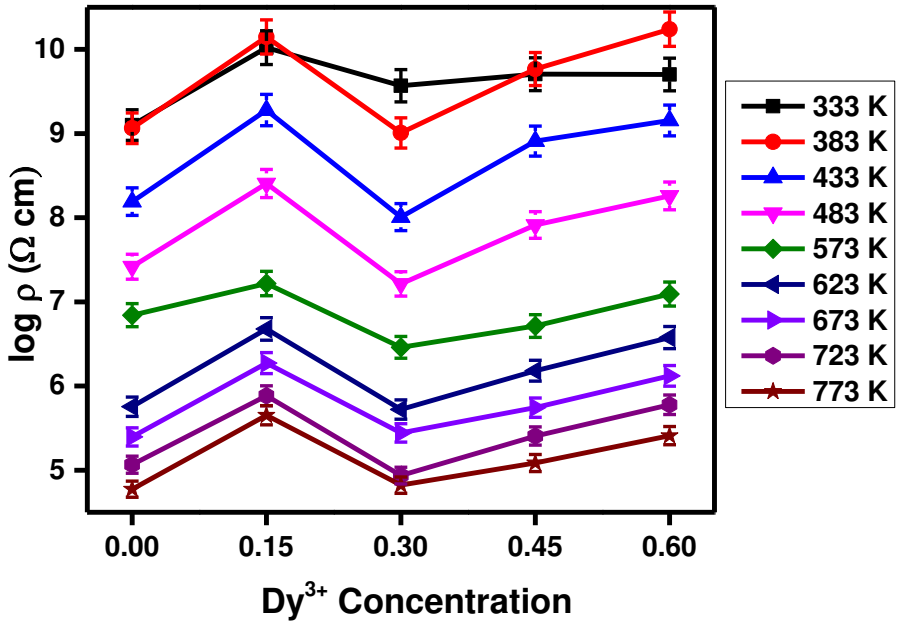

Fig. 9 Plots Dy^{3+} concentration (*x*) *versus* the log of resistivity for all the samples

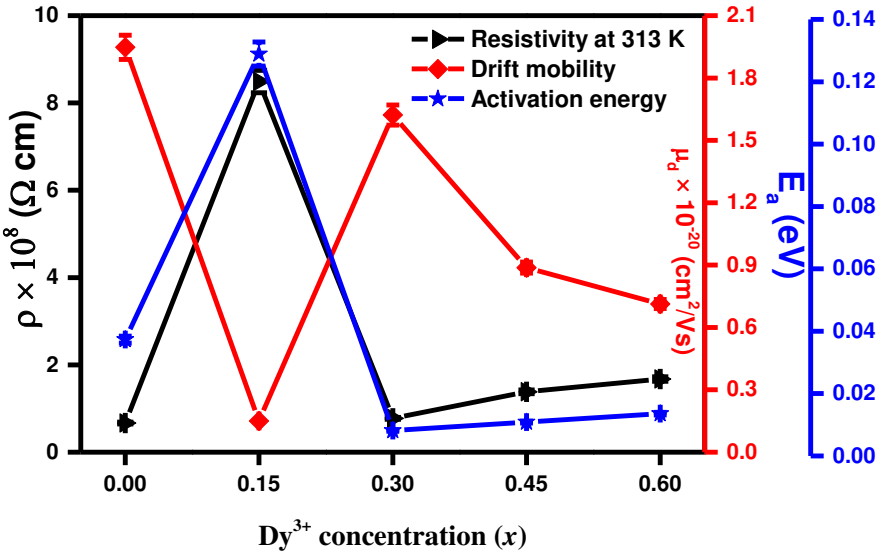

Fig. 10 The Dy^{3+} *vs.* electrical resistivity, drift mobility, and activation energy

4.6 Dielectric analysis of Dy^{3+} substituted $BiFeO_3$ ferrites

In the frequency range, 4 Hz – 8 MHz, the dielectric properties of Dy^{3+} substituted BFO ferrites at RT were examined. All of the sample's dielectric constants are reduced with increasing frequency and were constant at frequencies greater than 10 kHz, as depicted in Fig. 11. At low frequencies, a material's dielectric characteristics are primarily governed by its space charge and dipolar polarization. The openings of oxygen (V_O^{2+}) and bismuth (V_{Bi}^{3+}) in the Dy^{3+} substitutes BFO samples produce the space charges. At lower frequencies, the dipoles have enough time to line up with the applied electric field. At higher frequencies, however, the electric dipoles are unable to keep up with the fast alternating applied field, resulting in incomplete polarization. These findings are consistent with the literature's description of dipole relaxation [45]. It was also clear from Fig. 11 that the dielectric constant has a negative value. It may be because when an electric field is applied to the sample, free electrons in as-prepared ferrites oscillate with the fluctuation of the external electric field and generate a plasmonic state comparable to metal plasma oscillations. Negative permittivity is observed in pure and doped BFO samples with sufficient carrier concentration as a result [46, 47]. It was also noted from Fig. 11 that the dielectric constant was maximum for a sample having Dy^{3+} doping x = 0.45 and minimum for a BFO sample at low frequency.

The tangent loss (tan δ) decreased with increasing applied frequency up to 10 kHz and then increased with increasing the frequency, as seen in Fig. 12. There is a similar relationship

between frequency and tangent loss at lower frequencies. Based on Koop's idea, Maxwell and Wagner devised a two-layer model that may explain this type of behavior [22, 48, 49]. According to this theory, electrons are significantly more effective than grains at grain boundaries in the low-frequency range of magnetization electrical conduction, but grains are far more active than electrons in the higher frequency zone. The plots of log of frequency *versus ac* conductivity are shown in Fig. 13. The *ac* conductivity was increased at a low frequency up to the 10 kHz frequency and then at a higher frequency *ac* conductivity was reduced. It was also clear from Fig. 13 that the maximum *ac* conductivity was observed for x = 0.45. The electrical modulus is used to determine the impact of the produced sample's grain boundary, electrical conductivity, relaxation duration, electrode polarization, and conduction phenomena. Furthermore, this technique may be utilized to investigate many kinds of electrical processes that occur in the samples. The real (M') part of the electrical modulus of Dy^{3+} substituted BFO ferrites were studied in the frequency range of 4 Hz to 8 MHz at RT as shown in Fig. 14. The real (M') part of the electrical modulus remains constant at low frequency and increases with increasing frequency at high frequency. This behaviour of the real (M') component of the electrical modulus is caused by conduction processes and the existence of charge carrier short-range mobility.

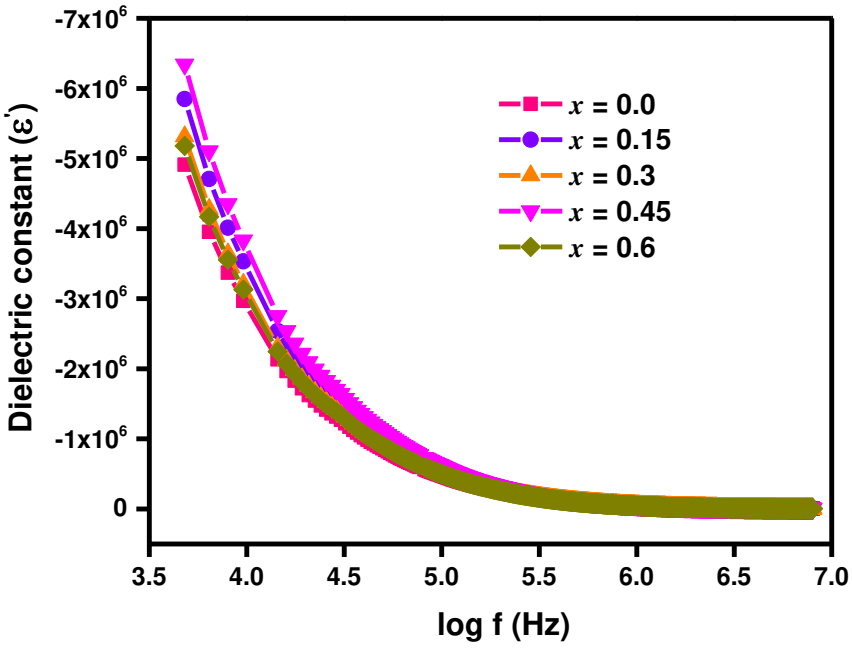

Fig. 11 Frequency-dependent dielectric constant for Dy^{3+} substituted $BiFeO_3$ samples

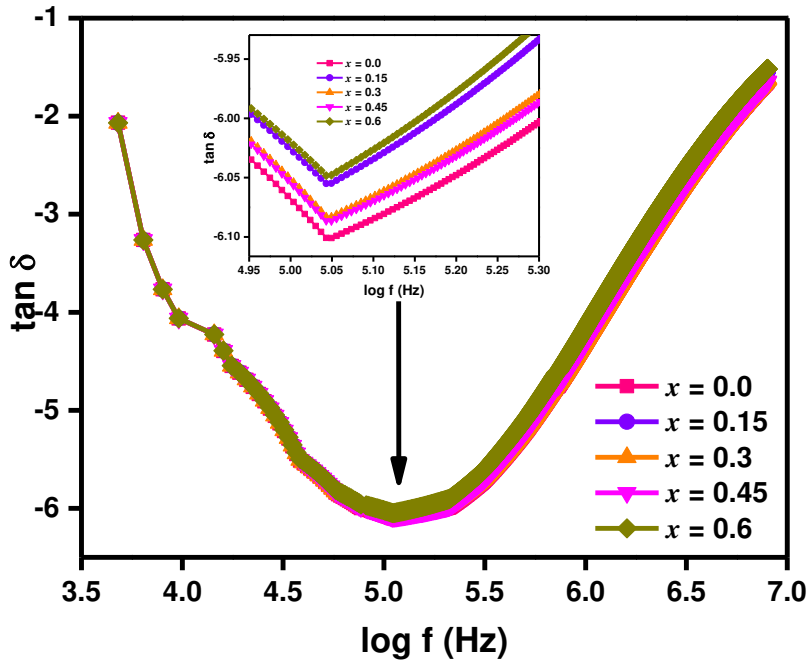

Fig. 12 Frequency-dependent tangent loss (tan δ) for Dy^{3+} substituted $BiFeO_3$ samples

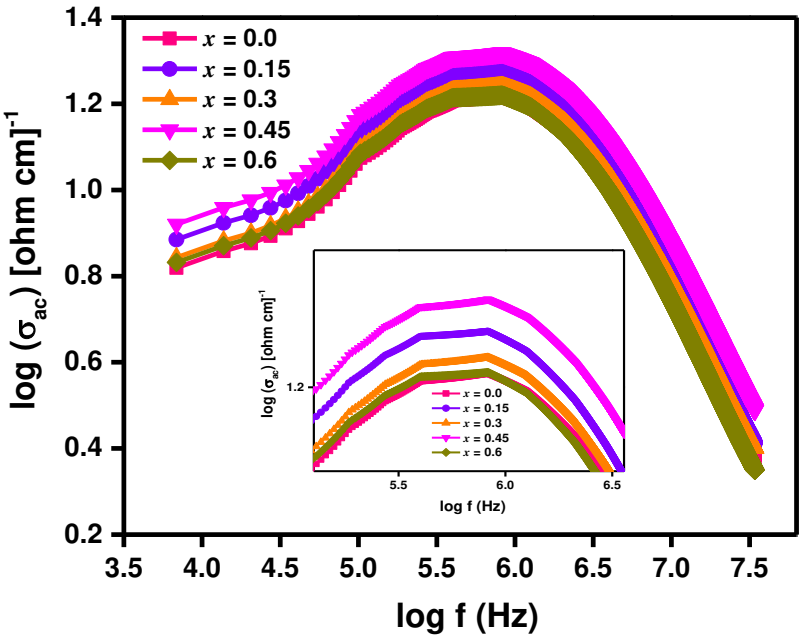

Fig. 13 Plots of log of frequency *versus ac* conductivity for all the samples

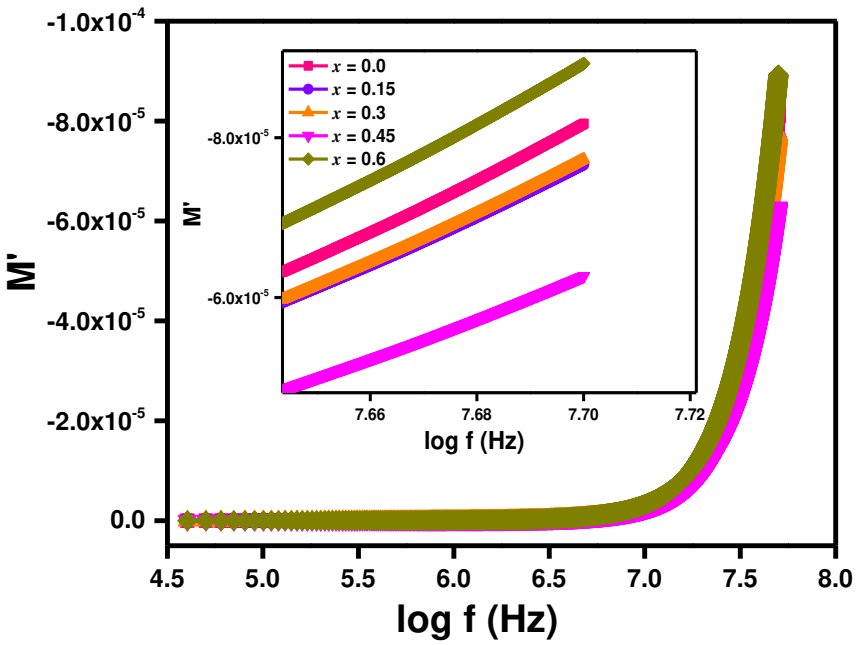

Fig. 14 The variation of log f *versus* real part of electrical modulus for all the samples

4.7 Ferroelectric analysis

Fig.15 shows ferroelectric hysteresis loop (*P*-*E*) of prepared samples $Bi_{1-x}Dy_xFeO_3$ (x = 0.0, 0.3 and 0.6) at RT. Because of the enormous coercive field and leakage current, the loops are not saturated [50]. The observed values of saturated polarization (P_S), electric polarization (E_C), and remnant polarization (P_r) are shown in Table 3. Fig. 15 shows that with increasing the Dy^{3+} substituted in BFO ferrites, the saturated polarization, electric polarization, and remnant polarization were decreased. Xu *et al*., [51] reported the irregularity in the ferroelectric properties with the substitution of Dy^{3+} ion in BFO ferrite. Muneeswaran *et al*., [52] observed that the remnant polarization was reduced with the substitution of Dy^{3+} ions in BFO ferrite. The presence of rare-earth ions raises the electronegativity difference for Bi^{3+} while simultaneously strengthening the Bi (RE)–O covalent connection, resulting in a greater off-center displacement in BFO. The ferroelectric characteristics of BFO should improve because the movement of the $6s^2$ lone pair electrons of Bi^{3+} relative to O^{2-} is the major source of ferroelectricity in BFO. It has also been noted that the defective dipole's ordering is critical for polarization enhancement.

Table 3 Dy^{3+} Concentration, *P*s, *P*r, and *H*c of as-prepared samples

x	*P*s×10^{-5} (μC/cm^2)	*P*r×10^{-5} (μC/cm^2)	*E*c (kV/cm)
0.0	7.42	4.91	1.74
0.3	6.95	3.49	1.53
0.6	6.01	3.38	1.42

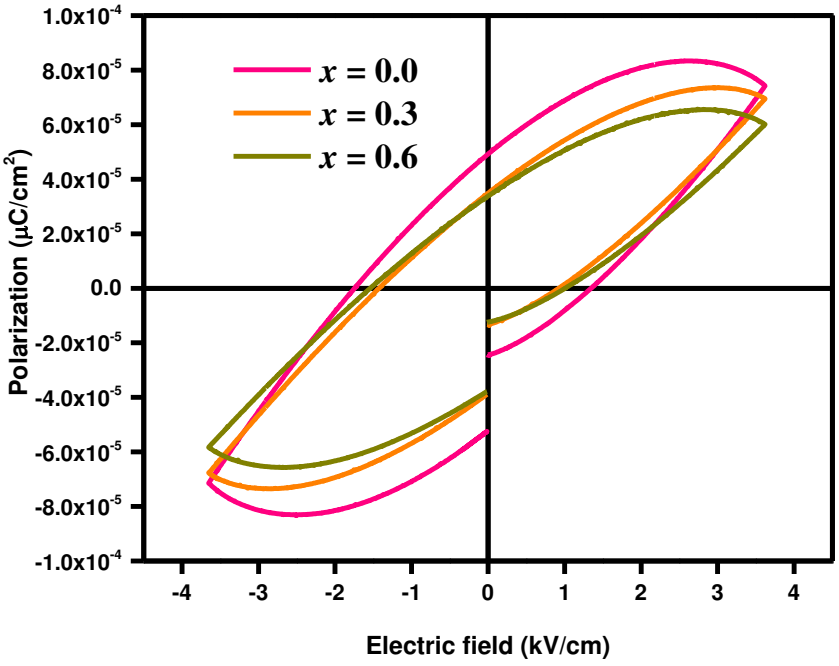

Fig. 15 *P-E* hysteresis loops of pure and $Bi_{1-x}Dy_xFeO_3$ with concentrations (x = 0.0, 0.3 and 0.6)

4.8 Magnetic properties of Dy^{3+} substituted $BiFeO_3$ ferrites

The S-shaped *M-H* loops for all as-synthesized samples are depicted in Fig. 16. Table 4 showed the saturation magnetization (M_S), retentivity (M_r), coercivity (H_C), and remanent ratio ($SQ = M_r/M_S$). Because of the increase in molecular weight of all samples as well as cation redistribution at the sub-lattice, saturation magnetization, and retentivity were minimum for x = 0.45, whereas coercivity was 220 Oe for x = 0.45 (Table 4). The remanent ratio was maximum for the sample x = 0.45. Xu *et al.*, [51] reported irregular change in magnetization with the addition of Dy^{3+} doping in BFO ferrite. The suppression of increased canting angles and inhomogeneous magnetic spin matrix could be the cause of magnetization variation and improvements with Dy^{3+} doping. The pure $BiFeO_3$ is a G-type structural antiferromagnet with a long-wavelength spiral modulation that prevents from appearing any net magnetization. Dy^{3+}

doping suppresses the spatially modulated spiral structure and causes the structural transition. Furthermore, the Dy^{3+} ion contains unpaired electrons, and as a result of the influence of these unpaired electrons, increased magnetic interaction is expected to occur, resulting in higher magnetization [24, 26]. The Bohr magneton (n_B) was determined using the following equation [35];

$$n_B = \frac{M \times M_S}{5585 \times d_X} \quad (16)$$

where "*M*" is the molecular weight, "d_X" is X-ray density and "*M*s" is saturation magnetization. The minimum Bohr magneton was 0.040 for $x = 0.45$ (Table 4). The anisotropy constant (K) was calculated using the relation [35];

$$K = \frac{H_C \times M_S}{0.96} \quad (17)$$

The smaller anisotropy constant was 1445.58 for $x = 0.45$. The initial permeability (μ_i) was estimated using equation (18) [35] and is reported in Table 4.

$$\mu_i = \frac{M_S^2 \times D}{K} \quad (18)$$

With the inclusion of Dy^{3+} ions, the initial permeability was reduced to a minimum of 1.504 for $x = 0.45$ as compared to doped samples. Microwave frequency was calculated using the relation $\omega_m = 8\pi^2 M_s \gamma$, where γ is a gyromagnetic fraction with the significance of 2.8 MHz/Oe [53-57]. It was clear from the above relation the microwave frequency is directly proportional to the saturation magnetization and the greater the saturation magnetization larger will be the microwave frequency. The applied field *versus* microwave frequency is depicted in Fig. 17. The graphical representation of Dy^{3+} concentration (x) *versus* magnetic parameters is depicted in Fig. 18(a-d). The microwave frequency was a minimum of 1.39 GHz for $x = 0.45$ and a maximum of 2.88 GHz for the $x = 0.15$ sample as compared to other as-prepared samples.

Table 4 Magnetic parameters of as-prepared samples

x	***H*C (Oe)**	***SQ***	***M*r (emu/g)**	***M*s (emu/g)**	***n*B**	***K* (erg/cm³)**	***μ*i**	***ω*m (GHz)**
0.00	174.31	0.261	2.19	8.36	0.056	1517.94	1.326	1.84
0.15	234.38	0.227	2.96	13.03	0.086	3181.22	3.087	2.88
0.30	262.64	0.279	3.04	10.89	0.071	2979.32	2.371	2.41
0.45	220.63	0.287	1.81	6.29	0.040	1445.58	1.504	1.39
0.60	218.64	0.268	1.91	7.12	0.044	1621.58	1.528	1.57

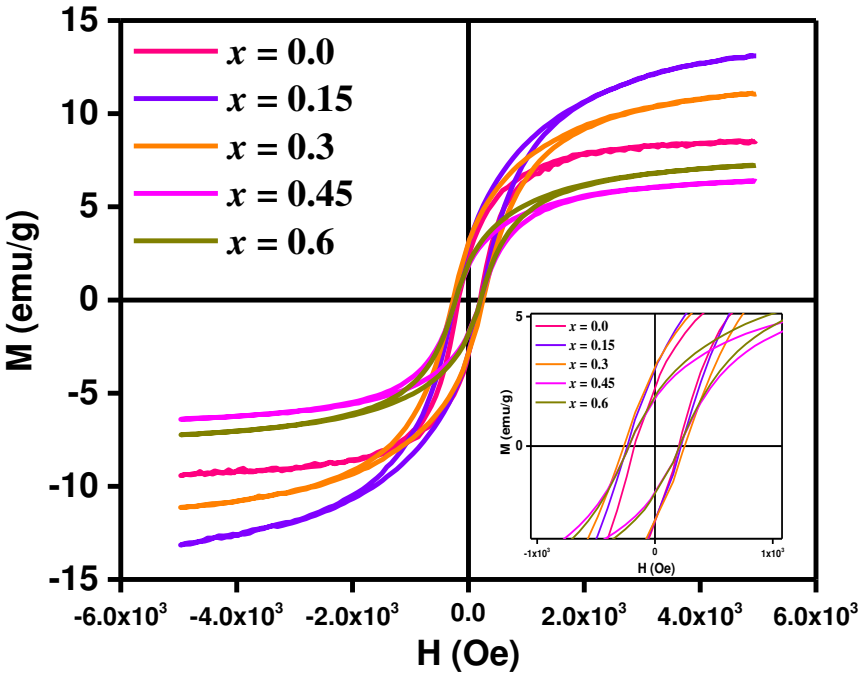

Fig. 16. *M-H* loops for all the as-prepared samples

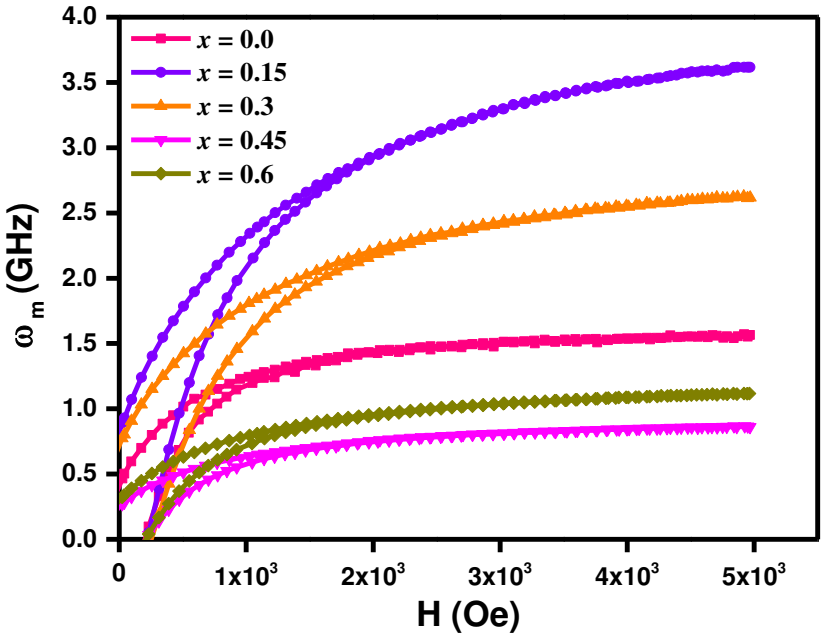

Fig. 17. Applied field *versus* microwave frequency for all the samples

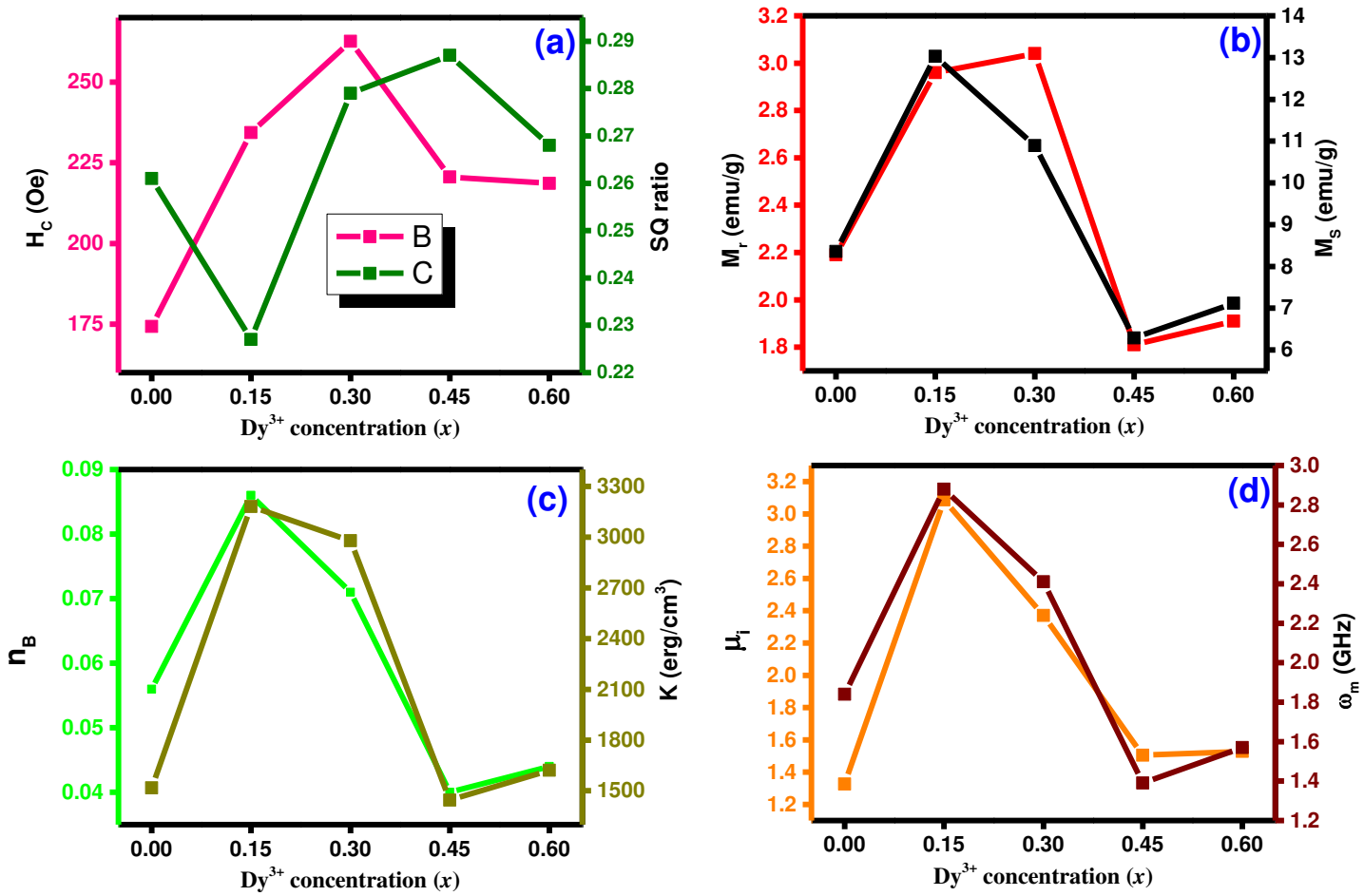

Fig. 18 Dy^{3+} concentration (x) *versus* **(a)** coercivity and remanent ratio **(b)** retentivity and saturation magnetization **(c)** Bohr magneton and anisotropy constant **(d)** initial permeability and microwave frequency of all the samples

5 Conclusions

Bismuth ferrite having chemical formula $Bi_{1-x}Dy_xFeO_3$ at (x = 0.00, 0.15, 0.30, 0.45, and 0.60) were prepared using the sol-gel auto combustion technique. The structure parameters and peak shift were observed with the substitution of dysprosium (Dy^{3+}) in bismuth ferrite (BFO). Moreover, the absorption peaks at 527 cm^{-1}, 533 cm^{-1} and 523 cm^{-1} for (x = 0.0, 0.30 and 0.60), respectively are associated with Fe–O stretching. The change in X-ray diffraction (XRD) parameters and absorption bands have confirmed the substitution of Dy^{3+} ion in the BFO lattice. The maximum energy bandgap (E_g) was 2.81 eV for x = 0.30. The minimum DC resistivity is 0.775×10^8 Ω cm for x = 0.30 at 313 K. The dielectric constants are reduced with increasing frequency and remain constant at a higher frequency. The saturation magnetization was 10.89

emu/g and retentivity has value 3.04 emu/g for the $x = 0.30$. The microwave frequency was 2.41 GHz for $x = 0.30$. Therefore, the as-prepared samples are microwave devices.

References

[1] A. Das, N. Khamaru, S. Bandyopadhyay, S. Chatterjee, D. Das, Enhanced magnetoelectric coupling in dysprosium-doped $BiFeO_3$ on the formation of nanocomposite with $SrFe_{12}O_{19}$, Journal of Alloys and Compounds, 859 (2021) 157821.

[2] S.D. Waghmare, S.D. Raut, B.G. Ghule, V.V. Jadhav, S.F. Shaikh, A.M. Al-Enizi, M. Ubaidullah, A. Nafady, B.M. Thamer, R.S. Mane, Pristine and palladium-doped perovskite bismuth ferrites and their nitrogen dioxide gas sensor studies, Journal of King Saud University-Science, 32 (2020) 3125-3130.

[3] S. Rizwan, S.U. Awan, S. Irfan, Room-temperature ferromagnetism in Gd and Sn co-doped bismuth ferrite nanoparticles and co-doped $BiFeO_3$/MXene (Ti_3C_2) nanohybrids for spintronics applications, Ceramics International, 46 (2020) 29011-29021.

[4] A. Singh, L.K. Meena, V.V. Dhawale, S. Singhal, S. Singh, S. Yadav, Comparative Studies of Electrical Properties of MFS and MIS Capacitors for Non-Volatile Memory Applications, in: 2020 International Conference on Electrical and Electronics Engineering (ICE3), IEEE, 2020, pp. 131-135.

[5] A. Queraltó, R. Frohnhoven, S. Mathur, A. Gómez, Intrinsic piezoelectric characterization of BiFeO3 nanofibers and its implications for energy harvesting, Applied Surface Science, 509 (2020) 144760.

[6] A. Kumar, K. Yadav, Magnetic, magnetocapacitance and dielectric properties of Cr doped bismuth ferrite nanoceramics, Materials Science and Engineering: B, 176 (2011) 227-230.

[7] Z.J. Li, Z.L. Hou, W.L. Song, X.D. Liu, W.Q. Cao, X.H. Shao, M.S. Cao, Unusual continuous dual absorption peaks in Ca-doped $BiFeO_3$ nanostructures for broadened microwave absorption, Nanoscale, 8 (2016) 10415-10424.

[8] G. Catalan, J.F. Scott, Physics and applications of bismuth ferrite, Advanced materials, 21 (2009) 2463-2485.

[9] L. Chen, L. Zheng, Y. He, J. Zhang, Z. Mao, X. Chen, The local distortion and electronic behavior in Mn doped $BiFeO_3$, Journal of Alloys and Compounds, 633 (2015) 216-219.

[10] J.H. Xu, H. Ke, D.C. Jia, W. Wang, Y. Zhou, Low-temperature synthesis of $BiFeO_3$ nanopowders via a sol–gel method, Journal of Alloys and Compounds, 472 (2009) 473-477.

[11] B.L. Cushing, V.L. Kolesnichenko, C.J. O'connor, Recent advances in the liquid-phase syntheses of inorganic nanoparticles, Chemical Reviews, 104 (2004) 3893-3946.

[12] I. ALIa, N. Amin, A. REHMAN, M. Akhtar, M. Fatima, K. Mahmood, A. ALIa, G. Mustafa, M. Hasan, A. Bibi, ELECTRICAL AND MAGNETIC PROPERTIES OF $BaCo_xCd_{2-x}Fe_{16}O_{27}$ W-TYPE HEXAFERRITES ($0 \leq x \leq 0.5$), Digest Journal of Nanomaterials Biostructures, 15 (2020).

[13] N. Amin, M. Akhtar, M. Sabir, K. Mahmood, A. ALIa, G. Mustafa, M. Hasan, A. Bibi, M. Iqbal, F. Iqbal, SYNTHESIS, STRUCTURAL AND OPTICAL PROPERTIES OF Zn-SUBSTITUTED Co W-FERRITES BY COPRECIPITATION METHOD, Journal of Ovonic Research, 16 (2020) 11-19.

[14] A. Aslam, A.U. Rehman, N. Amin, M.A. un Nabi, Q. ul ain Abdullah, N. Morley, M.I. Arshad, H.T. Ali, M. Yusuf, Z. Latif, Lanthanum doped $Zn_{0.5}Co_{0.5}La_xFe_{2-x}O_4$ spinel ferrites synthesized via co-precipitation route to evaluate structural, vibrational, electrical, optical, dielectric, and thermoelectric properties, Journal of Physics and Chemistry of Solids, 154 (2021) 110080.

[15] Q.H. Jiang, C.W. Nan, Z.J. Shen, Synthesis and properties of multiferroic La-modified $BiFeO_3$ ceramics, Journal of the American Ceramic Society, 89 (2006) 2123-2127.

[16] R. Zakir, S.S. Iqbal, A.U. Rehman, S. Nosheen, T.S. Ahmad, N. Ehsan, F. Inam, Spectral, electrical, and dielectric characterization of Ce-doped Co-Mg-Cd spinel nano-ferrites synthesized by the sol-gel auto combustion method, Ceramics International, 47 (2021) 28575-28583.

[17] X. Yang, Y. Zhang, G. Xu, X. Wei, Z. Ren, G. Shen, G. Han, Phase and morphology evolution of bismuth ferrites via hydrothermal reaction route, Materials Research Bulletin, 48 (2013) 1694-1699.

[18] D. Maurya, H. Thota, K.S. Nalwa, A. Garg, $BiFeO_3$ ceramics synthesized by mechanical activation assisted versus conventional solid-state-reaction process: A comparative study, Journal of alloys and compounds, 477 (2009) 780-784.
[19] A. Sagdeo, P. Mondal, A. Upadhyay, A. Sinha, A. Srivastava, S. Gupta, P. Chowdhury, T. Ganguli, S. Deb, Correlation of microstructural and physical properties in bulk $BiFeO_3$ prepared by rapid liquid-phase sintering, Solid state sciences, 18 (2013) 1-9.
[20] B. Dhanalakshmi, K. Pratap, B.P. Rao, P.S. Rao, Effects of Mn doping on structural, dielectric and multiferroic properties of $BiFeO_3$ nanoceramics, Journal of Alloys and Compounds, 676 (2016) 193-201.
[21] M. Basiri, H. Shokrollahi, G. Isapour, Effects of La content on the magnetic, electric and structural properties of $BiFeO_3$, Journal of magnetism and magnetic materials, 354 (2014) 184-189.
[22] P.C. Sati, M. Kumar, S. Chhoker, M. Jewariya, Influence of Eu substitution on structural, magnetic, optical and dielectric properties of $BiFeO_3$ multiferroic ceramics, Ceramics International, 41 (2015) 2389-2398.
[23] R. Mishra, D.K. Pradhan, R. Choudhary, A. Banerjee, Effect of yttrium on improvement of dielectric properties and magnetic switching behavior in $BiFeO_3$, Journal of Physics: Condensed Matter, 20 (2008) 045218.
[24] G. Dhir, N. Verma, Enhanced magnetization in Dy-doped Bismuth ferrite nanoparticles, in: AIP Conference Proceedings, AIP Publishing LLC, 2020, pp. 020193.
[25] M. Arora, S. Chauhan, P. Sati, M. Kumar, S. Chhoker, Evidence of spin-two phonon coupling and improved multiferroic behavior of $Bi_{1-x}Dy_xFeO_3$ nanoparticles, Ceramics International, 40 (2014) 13347-13356.
[26] P.C. Sati, M. Arora, S. Chauhan, M. Kumar, S. Chhoker, Effect of Dy substitution on structural, magnetic and optical properties of $BiFeO_3$ ceramics, Journal of Physics and Chemistry of Solids, 75 (2014) 105-108.
[27] S.T. Zhang, Y. Zhang, M.H. Lu, C.L. Du, Y.F. Chen, Z.G. Liu, Y.Y. Zhu, N.B. Ming, X. Pan, Substitution-induced phase transition and enhanced multiferroic properties of $Bi_{1-x}La_xFeO_3$ ceramics, Applied Physics Letters, 88 (2006) 162901.
[28] G. Yuan, S.W. Or, J. Liu, Z. Liu, Structural transformation and ferroelectromagnetic behavior in single-phase $Bi_{1-x}Nd_xFeO_3$ multiferroic ceramics, Applied Physics Letters, 89 (2006) 052905.
[29] J. Liu, L. Fang, F. Zheng, S. Ju, M. Shen, Enhancement of magnetization in Eu doped $BiFeO_3$ nanoparticles, Applied Physics Letters, 95 (2009) 022511.
[30] N. Amin, M.S.U. Hasan, Z. Majeed, Z. Latif, M.A. un Nabi, K. Mahmood, A. Ali, K. Mehmood, M. Fatima, M. Akhtar, Structural, electrical, optical and dielectric properties of yttrium substituted cadmium ferrites prepared by Co-Precipitation method, Ceramics International, 46 (2020) 20798-20809.
[31] J. Cyriac, S. Augustine, N. Kalarikkal, S. Mukherjee, M. Ahmed, P. Nambissan, Dysprosium-substitution-induced structural changes of multiferroic nanocrystalline bismuth ferrite and the investigation through positron annihilation and other studies, Physica B: Condensed Matter, 599 (2020) 412431.
[32] N. Amin, A. Razaq, A.U. Rehman, K. Hussain, M. Nabi, N. Morley, M. Amami, A. Bibi, M.I. Arshad, K. Mahmood, Transport properties of Ce-doped Cd ferrites $CdFe_{2-x}Ce_xO_4$, Journal of Superconductivity and Novel Magnetism, 34 (2021) 2945-2955.
[33] A. Aslam, A.U. Rehman, N. Amin, M. Amami, M. Nabi, H. Alrobei, M. Asghar, N. Morley, M. Akhtar, M.I. Arshad, Sol–Gel auto-combustion preparation of M^{2+}= Mg^{2+}, Mn^{2+}, Cd^{2+} substituted $M_{0.25}Ni_{0.15}Cu_{0.25}Co_{0.35}Fe_2O_4$ ferrites and their characterizations, Journal of Superconductivity and Novel Magnetism, 35 (2022) 473-483.
[34] P. Uniyal, K. Yadav, Observation of the room temperature magnetoelectric effect in Dy doped $BiFeO_3$, Journal of Physics: Condensed Matter, 21 (2008) 012205.
[35] K. Hussain, A. Bibi, F. Jabeen, N. Amin, K. Mahmood, A. Ali, M.Z. Iqbal, M. Arshad, Study of structural, optical, electrical and magnetic properties of Cu^{2+} doped $Zn_{0.4}Co_{0.6-x}Ce_{0.1}Fe_{1.9}O_4$ spinel ferrites, Physica B: Condensed Matter, 584 (2020) 412078.

[36] A. Aslam, A. Razzaq, S. Naz, N. Amin, M.I. Arshad, M. Nabi, A. Nawaz, K. Mahmood, A. Bibi, F. Iqbal, Impact of lanthanum-doping on the physical and electrical properties of cobalt ferrites, Journal of Superconductivity and Novel Magnetism, 34 (2021) 1855-1864.
[37] T. Vigneswari, P. Raji, Structural and magnetic properties of calcium doped nickel ferrite nanoparticles by co-precipitation method, Journal of Molecular Structure, 1127 (2017) 515-521.
[38] S.K. Srivastav, N. S. Gajbhiye, Low temperature synthesis, structural, optical and magnetic properties of bismuth ferrite nanoparticles, Journal of the American Ceramic Society, 95 (2012) 3678-3682.
[39] H. Ke, W. Wang, Y. Wang, J. Xu, D. Jia, Z. Lu, Y. Zhou, Factors controlling pure-phase multiferroic $BiFeO_3$ powders synthesized by chemical co-precipitation, Journal of Alloys and Compounds, 509 (2011) 2192-2197.
[40] A. Marzoukia, H. Harzalia, F. Saida, A. Megriche, K. Zehani, L. Bessais, Optimization of the synthesis of multiferroic bismuth ferrite $BiFeO_3$ nanopowders by hydrothermal method, Journal of the Tunisian Chemical Society, 18 (2016) 38-42.
[41] H.T. Ali, M. Ramzan, M.I. Arshad, N.A. Morley, M.H. Abbas, M. Yusuf, A.U. Rehman, K. Mahmood, A. Ali, N. Amin, Tailoring the optical and magnetic properties of La-BaM hexaferrites by Ni substitution, Chinese Physics B, 31 (2022) 027502.
[42] B. Bhushan, A. Basumallick, N. Vasanthacharya, S. Kumar, D. Das, Sr induced modification of structural, optical and magnetic properties in $Bi_{1-x}Sr_xFeO_3$ (x = 0, 0.01, 0.03, 0.05 and 0.07) multiferroic nanoparticles, Solid State Sciences, 12 (2010) 1063-1069.
[43] K. Hussain, N. Amin, M.I. Arshad, Evaluation of structural, optical, dielectric, electrical, and magnetic properties of Ce^{3+} doped $Cu_{0.5}Cd_{0.25}Co_{0.25}Fe_{2-x}O_4$ spinel nano-ferrites, Ceramics International, 47 (2021) 3401-3410.
[44] Z. Yao, H. Li, M. Ma, R. Chu, Z. Xu, J. Hao, G. Li, Preparation and electrical properties of $(1-x)SrBi_2Nb_2O_9-xBiFeO_3$ lead-free piezoelectric ceramics, Ceramics International, 42 (2016) 5391-5396.
[45] T. Hussain, S.A. Siddiqi, S. Atiq, M. Awan, Induced modifications in the properties of Sr doped $BiFeO_3$ multiferroics, Progress in Natural Science: Materials International, 23 (2013) 487-492.
[46] G. Fan, Z. Wang, K. Sun, Y. Liu, R. Fan, Doping-dependent negative dielectric permittivity realized in mono-phase antimony tin oxide ceramics, Journal of Materials Chemistry C, 8 (2020) 11610-11617.
[47] K. Sun, J. Xin, Z. Wang, S. Feng, Z. Wang, R. Fan, H. Liu, Z. Guo, Weakly negative permittivity and low frequency dispersive behavior in graphene/epoxy metacomposites, Journal of Materials Science: Materials in Electronics, 30 (2019) 14745-14754.
[48] R. Mazumder, A. Sen, Effect of Pb-doping on dielectric properties of $BiFeO_3$ ceramics, Journal of Alloys and Compounds, 475 (2009) 577-580.
[49] Q. Li, S. Bao, Y. Liu, Y. Li, Y. Jing, J. Li, Influence of lightly Sm-substitution on crystal structure, magnetic and dielectric properties of $BiFeO_3$ ceramics, Journal of Alloys and Compounds, 682 (2016) 672-678.
[50] S. Sharif, G. Murtaza, F. Shaheen, A. Akhtar, M. Shafique, M. Piracha, S. Atiq, Effect of Y ions incorporation on structural, morphological and magnetic properties of $Bi_{1-x}Dy_xFeO_3$ for ferromagnetic applications, Bulletin of Materials Science, 44 (2021) 1-12.
[51] J. Xu, G. Ye, M. Zeng, Structure transition and enhanced multiferroic properties of Dy-doped BiFeO3, Journal of alloys and compounds, 587 (2014) 308-312.
[52] M. Muneeswaran, N. Giridharan, Effect of Dy-substitution on the structural, vibrational, and multiferroic properties of $BiFeO_3$ nanoparticles, Journal of Applied Physics, 115 (2014) 214109.
[53] A. Majeed, M.A. Khan, F. ur Raheem, A. Hussain, F. Iqbal, G. Murtaza, M.N. Akhtar, I. Shakir, M.F. Warsi, Structural elucidation and magnetic behavior evaluation of rare earth (La, Nd, Gd, Tb, Dy) doped BaCoNi-X hexagonal nano-sized ferrites, Journal of magnetism and magnetic materials, 408 (2016) 147-151.
[54] S. Gaba, A. Kumar, P.S. Rana, M. Arora, Influence of La^{3+} ion doping on physical properties of magnesium nanoferrites for microwave absorption application, Journal of Magnetism and Magnetic Materials, 460 (2018) 69-77.

[55] A.U. Rehman, N. Amin, M.B. Tahir, M.A. un Nabi, N. Morley, M. Alzaid, M. Amami, M. Akhtar, M.I. Arshad, Evaluation of spectral, optoelectrical, dielectric, magnetic, and morphological properties of RE^{3+} (La^{3+}, and Ce^{3+}) and Co^{2+} co-doped $Zn_{0.75}Cu_{0.25}Fe_2O_4$ ferrites, Materials Chemistry and Physics, 275 (2022) 125301.
[56] A.U. Rehman, N. Morley, N. Amin, M.I. Arshad, M.A. un Nabi, K. Mahmood, A. Ali, A. Aslam, A. Bibi, M.Z. Iqbal, Controllable synthesis of La^{3+} doped $Zn_{0.5}Co_{0.25}Cu_{0.25}Fe_{2-x}La_xO_4$ (x = 0.0, 0.0125, 0.025, 0.0375, 0.05) nano-ferrites by sol-gel auto-combustion route, Ceramics International, 46 (2020) 29297-29308.
[57] M.I. Arshad, M. Hasan, A.U. Rehman, M. Akhtar, N. Amin, K. Mahmood, A. Ali, T. Trakoolwilaiwan, N.T.K. Thanh, Structural, optical, electrical, dielectric, molecular vibrational and magnetic properties of La^{3+} doped Mg–Cd–Cu ferrites prepared by Co-precipitation technique, Ceramics International, 48 (2022) 14246-14260.